



Finite-element modeling of soft solids with liquid inclusions



Yuhao Wang, David L. Henann*

School of Engineering, Brown University, Providence, RI 02912, USA

ARTICLE INFO

Article history:

Received 21 May 2016

Received in revised form 31 May 2016

Accepted 1 June 2016

Available online 8 June 2016

Keywords:

Surface tension

Hyperelasticity

Composite

Finite-element method

ABSTRACT

Surface tension is an important factor in the behavior of fluids but typically has a minimal or negligible effect in solids. However, when a solid is soft and its characteristic dimension is small, forces due to surface tension can become important and significantly affect elastic deformation, leading to interesting elasto-capillary phenomena. We have developed a finite-element formulation accounting for surface tension and large deformations in three-dimensional settings and demonstrate the simulation capability by examining a class of problems involving fluid-filled droplet inclusions in a soft solid matrix. Specifically, we (1) consider the response of isolated droplets under far-field loading and (2) micromechanically model composite materials made up of a finite volume fraction of fluid-filled inclusions in a soft solid matrix. In the latter case, recent experimental work in the literature has shown that when the matrix material is sufficiently compliant, the presence of droplets leads to stiffening – counter to the intuitive notion of the presence of fluid-filled inclusions leading to a more compliant composite material. We show that our numerical simulation capability predicts all experimentally observed phenomena related to fluid-filled inclusions in soft solids. Furthermore, we consider the large-deformation response of composite materials with fluid-filled inclusions – a situation difficult to address using analytical methods.

© 2016 Elsevier Ltd. All rights reserved.

1. Introduction

In soft solids, volumetric elastic strain energy and surface energy can be comparable in scale, leading to interesting manifestations of elasto-capillary coupling [1, 2]. This is in contrast to typical idealizations of fluids and elastic solids, which assume that only surface energy in the case of fluids or only strain energy in the case of elastic solids contributes to the total free energy. The relative importance of these two energy contributions for a given problem may be quantified through the elasto-capillary number $\gamma/G\ell$, where γ is the (constant) surface energy density, G is the shear modulus, and ℓ is a characteristic length scale. This dimensionless number represents the ratio of the total surface energy – which scales as γA with

surface area A – to the elastic strain energy – which scales as GV with volume V . The ratio of volume to surface area then defines the characteristic length $\ell = V/A$. In the limit that $\gamma/G\ell \gg 1$, surface energy dominates, and we have fluid-like behavior. Conversely, in the limit $\gamma/G\ell \ll 1$, the contribution of surface energy is negligible, and the typical idealization of an elastic solid is valid. When the elasto-capillary number is in the range $10^{-1} \lesssim \gamma/G\ell \lesssim 10^1$, elasto-capillary coupling will be observed.

To make the preceding discussion more precise, in this work, we focus attention on solids with “fluid-like” surface behavior in that the creation and annihilation of surface area is accommodated through material moving back and forth between the surface and the bulk – rather than through the stretching of atomic bonds along the surface. Such a physical viewpoint is appropriate for the material systems considered in this work – i.e., soft amorphous solids, such as gels. As a consequence, the surface energy density per unit deformed surface area is constant and

* Corresponding author.

E-mail address: david_henann@brown.edu (D.L. Henann).

gives rise to a surface stress, which is constant, isotropic, and tensile, with magnitude – the surface tension – equal to the surface energy density. In this case, the terms surface energy density and surface tension may be used interchangeably; however, for more complex surface behavior, this terminology is not appropriate. For a deeper discussion of the differences between surface energy density, surface stress, and surface tension, see the seminal work of Gurtin and Murdoch [3] as well as several more recent works [4,5,2].

Recent work has demonstrated the importance of elasto-capillary coupling in soft solids in a variety of phenomena. Surface tension can drive deformation in soft solids [6–8] and modify contact, adhesion, and wetting behavior [9–12]. Surface tension can also drive the Rayleigh–Plateau instability [13]; introduce an energy barrier for cavitation [14–16] and surface instabilities, such as creasing and wrinkling [17,18], in soft solids; and play an important role in the electro-creasing and electro-cavitation instabilities in dielectric elastomers [19]. One recent observation of elasto-capillary coupling is in composite materials made up of a soft solid matrix with fluid-filled inclusions [20,21]. The presence of fluid-filled inclusions in a solid matrix is expected to decrease the stiffness of the composite material, since the fluid inside the inclusion has zero shear modulus and does not resist shape change, and this is indeed the case when the surface tension of the inclusion/matrix interface is negligible. However, as the surface tension becomes more important, the energy cost of changing the initially spherical shape of the inclusions increases. Hence in this limit, inclusions remain more spherical and cause stiffening of the soft composite material.

To model the response of fluid-filled droplets in a soft matrix, recent work has extended Eshelby's theory of inclusions [22] to account for the surface tension of the solid/liquid interface to describe how isolated fluid-filled droplets of radius R deform in response to far-field loading for different elasto-capillary numbers γ/GR [23]. This solution has then been used to analytically determine the infinitesimal shear modulus of a composite material made up of a soft solid matrix with a given volume fraction of fluid-filled droplets using a Mori–Tanaka approach [24, 21,25] and a three-phase, self-consistent approach [26, 27], and good agreement with experiments has been attained. To move beyond the small-deformation, linearized-kinematics response and determine the full stress–strain response of these composite materials, nonlinear, numerical methods are required. The purpose of this paper is to address this point. First, in Section 2, we generalize our finite-element approach for elasto-capillary problems in two dimensions [28] to three-dimensional settings, and in Section 3.1, we show that our approach well describes the experimentally measured response of isolated droplets [23]. In Section 3.2.1, we then employ the micromechanical modeling approach of Danielsson, Parsons, Parks, and Boyce [29–31] to model isotropic, composite materials with finite volume fractions of fluid-filled droplets, subjected to small deformations, and show that our approach agrees with both experimental measurements and analytical models of the infinitesimal shear

modulus. Finally, in Section 3.2.2, we consider the large-deformation response of the composite material and show that the large-deformation response for different droplet volume fractions and elasto-capillary numbers may be collapsed by accounting for the change in the infinitesimal shear modulus – an observation that may be rationalized through the physical picture of deformation amplification in the matrix introduced by Bergström and Boyce [32].

2. Governing equations and finite-element modeling approach

2.1. Continuum framework

We begin by briefly recapping the continuum modeling framework, which accounts for large deformations and surface tension. We consider a body B identified with the region of space it occupies in a fixed reference configuration and denote by \mathbf{X} an arbitrary material point of B . The referential body B then undergoes a motion $\mathbf{x} = \chi(\mathbf{X}, t)$ to the deformed body \mathcal{B} with deformation gradient given by $\mathbf{F} = \nabla \chi$, such that $J = \det \mathbf{F} > 0$, where ∇ represents the gradient with respect to the material point \mathbf{X} . The displacement and displacement gradient are denoted as $\mathbf{u}(\mathbf{X}, t) = \chi(\mathbf{X}, t) - \mathbf{X}$ and $\mathbf{H} = \nabla \mathbf{u} = \mathbf{F} - \mathbf{1}$, respectively, and the right and left Cauchy–Green deformation tensors are given by $\mathbf{C} = \mathbf{F}^T \mathbf{F}$ and $\mathbf{B} = \mathbf{F} \mathbf{F}^T$, respectively.

The boundary of the deformed body, $\mathcal{S} = \partial \mathcal{B}$, may be divided into an arbitrary set of complementary subsurfaces $\mathcal{S}_{\gamma n}$, $\mathcal{S} = \cup \mathcal{S}_{\gamma n}$, on which the deformation-independent surface tension γ may smoothly vary. The surface tension may also undergo discontinuities over the corresponding set of curves that form the boundaries of the subsurfaces, denoted collectively as \mathcal{C} . The deformed body is subjected to a system of external forces, consisting of a body force per unit deformed volume \mathbf{b}_0 distributed over the volume \mathcal{B} , a surface traction per unit deformed area \mathbf{t}_0 distributed over the surface \mathcal{S} , and a line force per unit deformed length \mathbf{s}_0 distributed over the system of curves \mathcal{C} . Then, following the discussion in our previous work [28], by introducing a vector test field \mathbf{w} , we may succinctly write the equations of equilibrium in the weak form as¹

$$\begin{aligned} \int_{\mathcal{B}} \mathbf{T} : \text{grad } \mathbf{w} \, dv + \int_{\mathcal{S}} \gamma \, \text{div}_{\mathcal{S}} \mathbf{w} \, da \\ = \int_{\mathcal{B}} \mathbf{b}_0 \cdot \mathbf{w} \, dv + \int_{\mathcal{S}} \mathbf{t}_0 \cdot \mathbf{w} \, da + \int_{\mathcal{C}} \mathbf{s}_0 \cdot \mathbf{w} \, ds, \end{aligned} \quad (2.1)$$

¹ For broader context, in the most general statement of the weak form of equilibrium (2.1) – appropriate for any surface behavior – the second term on the left-hand-side is given by $\int_{\mathcal{S}} \mathbf{T}_{\mathcal{S}} : \text{grad}_{\mathcal{S}} \mathbf{w} \, da$, where $\mathbf{T}_{\mathcal{S}}$ is the symmetric surface Cauchy stress tensor and the operator $\text{grad}_{\mathcal{S}}(\bullet)$ denotes the surface gradient in the deformed body. (See Equation (6) of Javili and Steinmann [5] for such a general statement of the weak form of equilibrium, albeit expressed referentially.) Then, for the case of hyperelastic surface behavior with a constant, deformation-independent surface energy density per unit deformed surface area γ , the surface Cauchy stress takes the constant and isotropic form $\mathbf{T}_{\mathcal{S}} = \gamma \mathbf{1}_{\mathcal{S}}$, where $\mathbf{1}_{\mathcal{S}}$ is the surface identity tensor and γ clearly plays the role of the surface tension (see Section 4.2 of Javili and Steinmann [5]). Hence, for this form of the surface Cauchy stress, we recover the specialized weak form of (2.1).

where \mathbf{T} is the symmetric Cauchy stress tensor. The operator $\text{grad}(\bullet)$ denotes the gradient, and the operator $\text{div}_s(\bullet)$ denotes the surface divergence [3,4] – both with respect to the point \mathbf{x} in the deformed body.

Finally, we introduce constitutive equations for the soft solid material. In the present work, we focus on matrix materials modeled as a nearly-incompressible Neo-Hookean solid, but this may easily be extended to more complex material models, such as the Gent model as in our previous work [28]. Defining the distortional left Cauchy–Green tensor, $\mathbf{B}_{\text{dis}} = J^{-2/3}\mathbf{B}$, and the distortional first stretch invariant, $\bar{I}_1 = \text{tr}(\mathbf{B}_{\text{dis}})$, we take the referential free energy density function to be

$$\psi = \frac{1}{2}G(\bar{I}_1 - 3) + \frac{1}{2}K(J - 1)^2, \quad (2.2)$$

where G and K are the ground-state shear and bulk moduli, respectively. Throughout, in order to model a nearly incompressible matrix material, we take $K/G = 100$. The Cauchy stress is then given by

$$\mathbf{T} = J^{-1} \frac{\partial \psi}{\partial \mathbf{F}} \mathbf{F}^\top = J^{-1}G \text{dev}(\mathbf{B}_{\text{dis}}) + K(J - 1)\mathbf{1}, \quad (2.3)$$

where $\text{dev}(\bullet)$ denotes the deviatoric part of a tensor. The first Piola (nominal) stress is related to the Cauchy stress through $\mathbf{S} = J\mathbf{T}\mathbf{F}^{-\top}$.

2.2. Finite-element implementation

The weak form of equilibrium (2.1) represents a suitable basis for a finite-element formulation. Following our previous work [28], the deformed body is approximated using finite elements, $\mathcal{B} = \cup \mathcal{B}^e$, and the nodal solution variable is taken to be the displacement, which is interpolated inside each element by

$$\mathbf{u} = \sum_A \mathbf{u}^A N^A, \quad (2.4)$$

with the index $A = 1, 2, \dots$ denoting the nodes of the element, \mathbf{u}^A the nodal displacements, and N^A the shape functions. By employing a Galerkin approach, in which the weighting field \mathbf{w} is interpolated by the same shape functions, standard arguments lead to the following element-level residuals:

$$\begin{aligned} (\mathbf{R}_u)^A = & - \int_{\mathcal{B}^e} \mathbf{T} \text{grad} N^A dv - \int_{\mathcal{S}^e} \gamma \text{grad}_s N^A da \\ & + \int_{\mathcal{B}^e} N^A \mathbf{b}_0 dv + \int_{\mathcal{S}^e} N^A \mathbf{t}_0 da + \int_{\mathcal{C}^e} N^A \mathbf{s}_0 ds, \end{aligned} \quad (2.5)$$

where the operator $\text{grad}_s(\bullet)$ denotes the surface gradient in the deformed body.

The non-standard term appearing in (2.5) is the contribution due to surface tension,

$$(\mathbf{R}_u^\gamma)^A = - \int_{\mathcal{S}^e} \gamma \text{grad}_s N^A da, \quad (2.6)$$

which hinges upon the calculation of the surface gradient of the shape functions – a calculation requiring elements of differential geometry [3,4]. We consider the face of

a general three-dimensional, isoparametric, continuum finite-element – for example, the four-node face of an eight-node, linear brick element or the six-node face of ten-node, quadratic tetrahedral element – and denote the number of face nodes as m . The position of a point on the face of a three-dimensional, isoparametric, continuum finite-element may be parametrized as

$$\mathbf{x}(\xi_1, \xi_2) = \mathbb{N}(\xi_1, \xi_2) [\mathbf{d}], \quad (2.7)$$

where $\mathbb{N}(\xi_1, \xi_2)$ is a $3 \times 3m$ -dimensioned matrix of interpolating functions – typically the element shape functions evaluated on the appropriate face of the element² – organized as shown in Box 1 with appropriate natural coordinates ξ_1 and ξ_2 , and $[\mathbf{d}]$ is a column vector of length $3m$ containing the *current* coordinates of the nodes associated with the element face, i.e.,

$$[\mathbf{d}] = [x_1^1 \ x_1^2 \ x_1^3 \ \cdots \ x_1^m \ x_2^m \ x_3^m]^\top. \quad (2.10)$$

The covariant basis vectors on the surface are then

$$\mathbf{g}_1 = \frac{\partial \mathbf{x}}{\partial \xi_1} = \left[\frac{\partial \mathbb{N}}{\partial \xi_1} \right] [\mathbf{d}] \quad \text{and} \quad \mathbf{g}_2 = \frac{\partial \mathbf{x}}{\partial \xi_2} = \left[\frac{\partial \mathbb{N}}{\partial \xi_2} \right] [\mathbf{d}], \quad (2.11)$$

and the covariant metric components are calculated as

$$[g_{ij}] = [\mathbf{g}_i \cdot \mathbf{g}_j] = \begin{bmatrix} E & F \\ F & G \end{bmatrix} \quad (2.12)$$

with

$$\begin{aligned} E &= \mathbf{g}_1 \cdot \mathbf{g}_1 = [\mathbf{d}]^\top \left[\frac{\partial \mathbb{N}}{\partial \xi_1} \right]^\top \left[\frac{\partial \mathbb{N}}{\partial \xi_1} \right] [\mathbf{d}], \\ G &= \mathbf{g}_2 \cdot \mathbf{g}_2 = [\mathbf{d}]^\top \left[\frac{\partial \mathbb{N}}{\partial \xi_2} \right]^\top \left[\frac{\partial \mathbb{N}}{\partial \xi_2} \right] [\mathbf{d}], \\ F &= \mathbf{g}_1 \cdot \mathbf{g}_2 = [\mathbf{d}]^\top \left[\frac{\partial \mathbb{N}}{\partial \xi_1} \right]^\top \left[\frac{\partial \mathbb{N}}{\partial \xi_2} \right] [\mathbf{d}]. \end{aligned} \quad (2.13)$$

Next, the contravariant metric components are

$$[g^{ij}] = [g_{ij}]^{-1} = \frac{1}{H^2} \begin{bmatrix} G & -F \\ -F & E \end{bmatrix} \quad (2.14)$$

with $H^2 = EG - F^2$, so that the contravariant basis vectors, calculated through $\mathbf{g}^i = g^{ij}\mathbf{g}_j$, are

$$\begin{aligned} \mathbf{g}^1 &= g^{11}\mathbf{g}_1 + g^{12}\mathbf{g}_2 \\ &= \frac{1}{H^2} \left(G \left[\frac{\partial \mathbb{N}}{\partial \xi_1} \right] [\mathbf{d}] - F \left[\frac{\partial \mathbb{N}}{\partial \xi_2} \right] [\mathbf{d}] \right), \\ \mathbf{g}^2 &= g^{21}\mathbf{g}_1 + g^{22}\mathbf{g}_2 \\ &= \frac{1}{H^2} \left(-F \left[\frac{\partial \mathbb{N}}{\partial \xi_1} \right] [\mathbf{d}] + E \left[\frac{\partial \mathbb{N}}{\partial \xi_2} \right] [\mathbf{d}] \right). \end{aligned} \quad (2.15)$$

² For illustrative purposes, consider the eight-node linear hexahedral element with $m = 4$ face nodes. The interpolating functions on a generic face of this element are

$$\begin{aligned} N^1(\xi_1, \xi_2) &= \frac{1}{4}(1 - \xi_1)(1 - \xi_2), & N^2 &= \frac{1}{4}(1 - \xi_1)(1 + \xi_2), \\ N^3(\xi_1, \xi_2) &= \frac{1}{4}(1 + \xi_1)(1 + \xi_2), & N^4 &= \frac{1}{4}(1 + \xi_1)(1 - \xi_2), \end{aligned} \quad (2.8)$$

with $-1 \leq \xi_1, \xi_2 \leq 1$.

$$\mathbb{N}(\xi_1, \xi_2) = \begin{bmatrix} N^1(\xi_1, \xi_2) & 0 & 0 & \cdots & N^m(\xi_1, \xi_2) & 0 & 0 \\ 0 & N^1(\xi_1, \xi_2) & 0 & \cdots & 0 & N^m(\xi_1, \xi_2) & 0 \\ 0 & 0 & N^1(\xi_1, \xi_2) & \cdots & 0 & 0 & N^m(\xi_1, \xi_2) \end{bmatrix}, \quad (2.9)$$

Box I.

The surface gradients of the interpolating functions, organized in a column vector of length $3m$, may then be calculated as

$$\begin{aligned} & \left[\frac{\partial \mathbb{N}}{\partial \xi_1} \right]^\top \mathbf{g}^1 + \left[\frac{\partial \mathbb{N}}{\partial \xi_2} \right]^\top \mathbf{g}^2 \\ &= \frac{1}{H^2} \left(G \left[\frac{\partial \mathbb{N}}{\partial \xi_1} \right]^\top \left[\frac{\partial \mathbb{N}}{\partial \xi_1} \right] [\mathbf{d}] - F \left[\frac{\partial \mathbb{N}}{\partial \xi_1} \right]^\top \left[\frac{\partial \mathbb{N}}{\partial \xi_2} \right] [\mathbf{d}] \right. \\ & \quad \left. - F \left[\frac{\partial \mathbb{N}}{\partial \xi_2} \right]^\top \left[\frac{\partial \mathbb{N}}{\partial \xi_1} \right] [\mathbf{d}] + E \left[\frac{\partial \mathbb{N}}{\partial \xi_2} \right]^\top \left[\frac{\partial \mathbb{N}}{\partial \xi_2} \right] [\mathbf{d}] \right). \end{aligned} \quad (2.16)$$

Finally, noting that the incremental area is $da = H d\xi_1 d\xi_2$ and organizing the surface tension contribution to the element-level residuals (2.6) as a column vector of length $3m$,

$$\mathbb{R}^\gamma = \left[(R_{u_1}^\gamma)^1 (R_{u_2}^\gamma)^1 (R_{u_3}^\gamma)^1 \cdots (R_{u_1}^\gamma)^m (R_{u_2}^\gamma)^m (R_{u_3}^\gamma)^m \right]^\top, \quad (2.17)$$

we may write \mathbb{R}^γ in the following form, which is amenable to implementation,

$$\begin{aligned} \mathbb{R}^\gamma = & - \int_\Gamma \gamma \frac{1}{H} \left(G \left[\frac{\partial \mathbb{N}}{\partial \xi_1} \right]^\top \left[\frac{\partial \mathbb{N}}{\partial \xi_1} \right] [\mathbf{d}] \right. \\ & - F \left[\frac{\partial \mathbb{N}}{\partial \xi_1} \right]^\top \left[\frac{\partial \mathbb{N}}{\partial \xi_2} \right] [\mathbf{d}] \\ & - F \left[\frac{\partial \mathbb{N}}{\partial \xi_2} \right]^\top \left[\frac{\partial \mathbb{N}}{\partial \xi_1} \right] [\mathbf{d}] \\ & \left. + E \left[\frac{\partial \mathbb{N}}{\partial \xi_2} \right]^\top \left[\frac{\partial \mathbb{N}}{\partial \xi_2} \right] [\mathbf{d}] \right) d\xi_1 d\xi_2, \end{aligned} \quad (2.18)$$

where Γ is the standard domain of integration for the natural coordinates of a given isoparametric element. The corresponding tangents are calculated through

$$(\mathbf{K}_{\mathbf{uu}}^\gamma)^{AB} = - \frac{\partial (\mathbf{R}_{\mathbf{u}}^\gamma)^A}{\partial \mathbf{u}^B}. \quad (2.19)$$

Since the current coordinates are interpolated with the same shape functions as the displacements, the tangents – expressed in the form of a $3m \times 3m$ -dimensioned matrix, \mathbb{K}^γ – are simply calculated as the derivative of the residuals \mathbb{R}^γ (2.18) with respect to the current nodal coordinates \mathbf{d} (2.10). This calculation is straightforward but, due to the dependence of the metric components, E , F , G , and H , on \mathbf{d} , quite lengthy and not reproduced here. The finite-element procedures have been implemented in Abaqus/Standard [33] using user-element (UEL) subroutines. We have developed a ten-node quadratic tetrahedral user-element and an eight-node linear hexahedral user-element for elasto-capillary

problems. Both elements have been verified and are made available online, but in the following section, we only report results using the quadratic tetrahedral element.³

3. Numerical simulations

In this section, we apply our three-dimensional simulation capability to problems involving fluid-filled droplets. We first consider isolated fluid-filled droplets in an elastic matrix and subjected to far-field loading. Then, we consider composite materials with finite volume fractions of fluid-filled droplets under both small-deformation and large-deformation settings.

3.1. Isolated fluid-filled droplets

First, in order to demonstrate that our three-dimensional numerical simulation capability for elasto-capillary problems is capable of replicating experimental measurements and analytical results in the linear regime, we consider the work of Style et al. [20,23] on isolated, fluid-filled droplets in an elastic matrix. In their experiments, they considered isolated droplets of different radii R filled with an ionic liquid in a silicone gel matrix. The matrix material was then subjected to far-field, non-equibiaxial deformation. They observed that smaller droplets – which are associated with a higher elasto-capillary number γ/GR – were more resistant to shape change under far-field deformation, i.e., small droplets are stiffer than large droplets.

In our simulations, we consider a geometry in the shape of a cube with undeformed side length L with an initially spherical droplet of radius R at its center, as shown in Fig. 1(a). The side length of the cubic domain is taken to be $L = 8.5R$, so that it is significantly larger than the droplet and hence approximates an infinite matrix. The matrix material is meshed using 79,484 quadratic, tetrahedral elements. The full mesh is not shown in Fig. 1(a), but the mesh on the droplet/matrix interface is pictured to give a sense of the resolution. The applied far-field deformation consists of a large tensile stretch in the 1-direction, quantified by $\lambda_1^\infty > 1$, and a smaller compressive stretch in the 2-direction, represented by $\lambda_2^\infty < 1$. The 3-direction remains unconstrained, so that the far-field normal stress component in the 3-direction remains zero. In order to achieve the prescribed far-field deformation, the two faces of the cube with surface normal in the 1-direction are displaced relative to each other by an amount

³ This choice is based solely on considerations of mesh generation for the problems considered in Section 3 and is not related to the accuracy of the hexahedral element. The numerical performance of the linear hexahedral elasto-capillary element is comparable to that of its standard, strictly-mechanical counterpart.

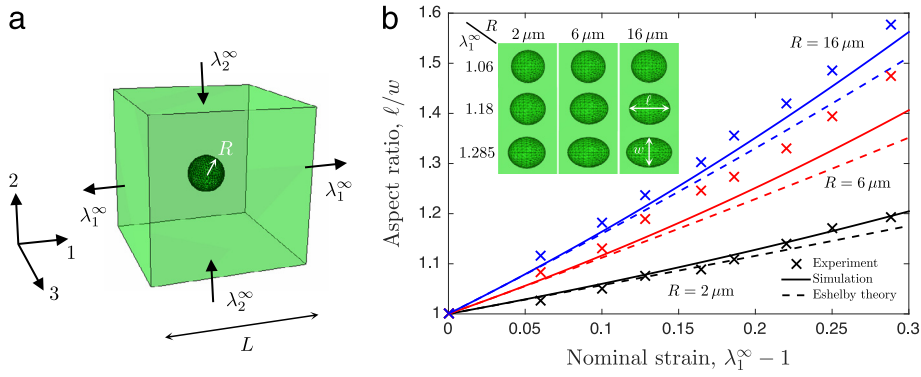


Fig. 1. (a) Finite-element configuration for the isolated fluid-filled droplet simulations. (b) Relation between the applied far-field nominal strain, $(\lambda_1^\infty - 1)$, and droplet aspect ratio ℓ/w for initial droplet radii of $R = 2, 6$, and $16 \mu\text{m}$. Solid lines are simulation results, symbols are experimental results from Style et al. [20], and the dashed lines are the modified Eshelby theory of Style et al. [23]. The inset shows the deformed shape of the droplet for each initial droplet radius and applied stretches in the 1-direction of $\lambda_1^\infty = 1.06, 1.18$, and 1.285 . These values were chosen to be comparable to Figure 1 of Style et al. [20].

$\Delta_1 = (\lambda_1^\infty - 1)L$, and similarly, a relative displacement of $\Delta_2 = (\lambda_2^\infty - 1)L$ is applied to the two faces with surface normal in the 2-direction, as indicated in Fig. 1(a). We take the ratio of the nominal strains to be $(\lambda_2^\infty - 1)/(\lambda_1^\infty - 1) = -0.24$ throughout the loading process, which follows the reported experiments of Style et al. [20]. We take the droplet to be filled with an incompressible fluid, and in order to constrain the volume of the fluid-filled droplet to be constant throughout our simulations, we utilize the built-in fluid-filled-cavity constraint in Abaqus/Standard [33]. The droplet/matrix interface has a surface tension of γ but is otherwise unconstrained and traction-free. Regarding material properties, following Style et al. [20], we take the shear modulus of the matrix to be $G = 566.67 \text{ Pa}$ (so that the bulk modulus of the matrix is $K = 100G = 56.67 \text{ kPa}$) and the surface tension of the droplet/matrix interface to be $\gamma = 3.6 \text{ mJ/m}^2$.

We have considered three different droplet radii of $R = 2, 6$, and $16 \mu\text{m}$, corresponding to elasto-capillary numbers of $\gamma/GR = 3.18, 1.06$, and 0.3971 , respectively. The far-field loading causes the droplet to change shape from a sphere to a tri-axial ellipsoid. The simulated deformed shape of the droplet in the 1–2-plane at far-field stretches of $\lambda_1^\infty = 1.06, 1.18$, and 1.285 and all three droplet radii considered are shown in the inset of Fig. 1(b) (see Figure 1 of Style et al. [20] to compare with the experimentally measured deformed droplet shapes at similar levels of far-field strain). We define the aspect ratio of the deformed droplet in the 1–2-plane as the length of the axis in the 1-direction, ℓ , divided by the length of the axis in the 2-direction, w . Not only does the aspect ratio of the droplet increase with λ_1^∞ for fixed droplet size, as indicated in each column, but it also increases with the undeformed radius of the droplet (decreasing elasto-capillary number) at fixed far-field stretch, as shown in each row, which indicates that the surface tension indeed plays an essential role in determining the amount of deformation. For larger elasto-capillary number, the increased role of surface tension resists the creation of new droplet surface area, favoring a more spherical shape and leading to a smaller aspect ratio upon deformation. The simulated aspect ratio as a function of the far-field nominal strain, $\lambda_1^\infty - 1$, is plotted as solid lines for each droplet

radius, along with the corresponding experimental data of Style et al. [20] as symbols in Fig. 1(b), and the agreement is good well into the large-deformation regime (nominal strains up to 0.3). Eshelby's theory for inhomogeneities subjected to far-field loading has been modified by Style et al. [23] to account for surface tension. Using the modified theory, the aspect ratio of a fluid-filled droplet in an incompressible matrix, subjected to non-equi-biaxial far-field loading, was derived to be

$$\frac{\ell}{w} = \frac{6 + 5(\gamma/GR) + 10(\lambda_1^\infty - 1)}{6 + 5(\gamma/GR) + 10(\lambda_2^\infty - 1)}. \quad (3.1)$$

We also plot (3.1) as a dashed line in Fig. 1(b). The analytical and simulated results are almost identical well into the moderate-deformation regime (nominal strain up to approximately 0.1), which verifies our simulation capability in the small deformation limit. For larger deformations, the simulations are able to account for much of the difference between the experiments and the linear theory, since no linearizing approximations are made in the simulations.

3.2. Composites with fluid-filled droplets

3.2.1. Infinitesimal composite shear modulus

Next, we extend our work to model composites with finite volume fractions ϕ of spherical, fluid-filled droplets with radius R randomly distributed in a soft solid matrix with ground-state shear modulus G , shown schematically in Fig. 2(a). The surface tension of the droplet/matrix interface is γ . First, we consider the effect of droplet volume fraction ϕ and elasto-capillary number γ/GR on the infinitesimal composite shear modulus G_c . Intuitively, one expects that as the volume fraction of fluid-filled droplets in a composite material is increased, the composite stiffness should decrease, since the shear stiffness of the fluid in the droplets is zero. Indeed, this is the case if surface tension is negligible. However, when surface tension plays an important role, we have seen from our study of isolated droplets that droplets resist shape change, preferring a spherical shape in order to minimize the interfacial area. Therefore, the presence of droplets

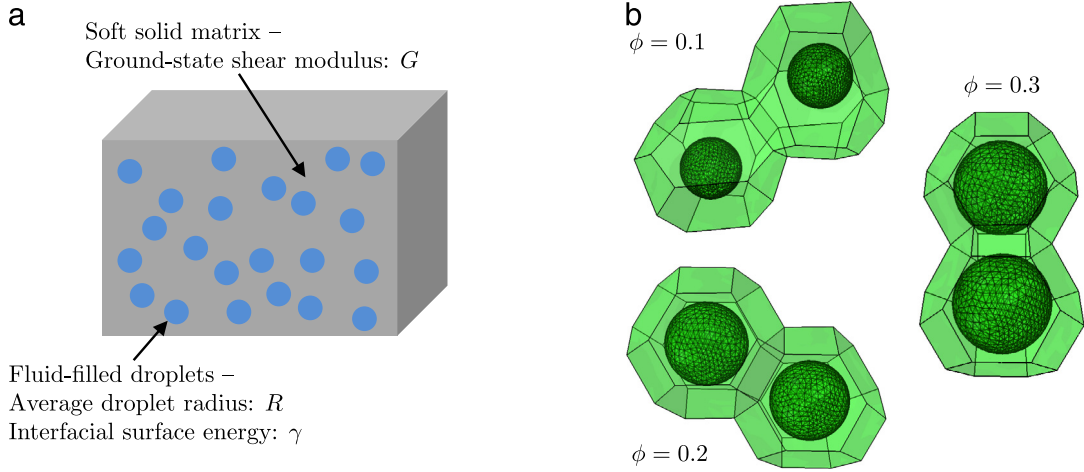


Fig. 2. (a) Schematic of the composite material made up of a soft solid matrix with ground state shear modulus G and fluid-filled inclusions with radius R and interfacial surface tension γ . (b) Two-droplet representative volume elements (RVEs) for droplet volume fractions of $\phi = 0.1, 0.2, 0.3$. For each volume fraction, a second randomly-generated, two-particle RVE configuration is considered but not shown.

should be expected to cause stiffening when the elastocapillary number is sufficiently high.

To model three-dimensional, isotropic composite materials, made up of finite volume fractions of randomly dispersed fluid-filled droplets, we employ the micromechanical modeling approach of Danielsson, Parsons, Parks, and Boyce [29–31]. This approach is based upon the use representative volume elements (RVEs) consisting of a prescribed number of randomly dispersed droplets to approximate an isotropic continuum material. The RVEs are generated by first *randomly* positioning the chosen number of droplets in a reference unit cube with the radius of the droplets R chosen to achieve the desired droplet volume fraction ϕ . The unit cube is then replicated 26 times with each image offset from the original cube by linear combinations of the basis vectors aligned with the edges of the unit cube. A Voronoi tessellation is then performed, and the Voronoi volumes for the replica droplets are eliminated (see Figure 5-3 of Parsons [31] for a schematic representation of this process in two-dimensions). The result is an RVE, consisting of the desired number of droplets together with their associated Voronoi volume of matrix material, which is capable of being tiled to fill space. Examples of two-droplet RVEs for droplet volume fractions of $\phi = 0.1, 0.2$, and 0.3 are shown in Fig. 2(b). To verify that our results are indeed representative of an isotropic composite material, we consider a second randomly-generated, two-droplet RVE for each droplet volume fraction, which are not pictured in Fig. 2(b). A surface tension of γ is associated with each droplet/matrix interface, and the volume of each droplet is held fixed using the fluid-filled-cavity constraint as in the previous section. Each RVE is meshed with quadratic tetrahedral elements with roughly 5000–6000 elements per Voronoi cell. The mesh on the droplet/matrix interface of each RVE in Fig. 2(b) is shown for reference.

Following Danielsson et al. [29], periodicity is maintained and the far-field loading is applied through the use of nine generalized degrees of freedom, which represent

the Cartesian components of the macroscopic displacement gradient, denoted with an overbar, i.e.,

$$[\bar{\mathbf{H}}] = \begin{bmatrix} \bar{H}_{11} & \bar{H}_{12} & \bar{H}_{13} \\ \bar{H}_{21} & \bar{H}_{22} & \bar{H}_{23} \\ \bar{H}_{31} & \bar{H}_{32} & \bar{H}_{33} \end{bmatrix}. \quad (3.2)$$

These nine generalized degrees of freedom then relate the displacements of periodic pairs of nodes through a system of constraint equations. Specifically, for a periodic pair of nodes, denoted as A and B, with referential coordinates \mathbf{X}^A and \mathbf{X}^B , the nodal displacements \mathbf{u}^A and \mathbf{u}^B are related through

$$\mathbf{u}^B - \mathbf{u}^A = \bar{\mathbf{H}}(\mathbf{X}^B - \mathbf{X}^A), \quad (3.3)$$

where the same nine components of $\bar{\mathbf{H}}$ are used for all periodic pairs in the finite-element calculation. Danielsson et al. [29] showed using the principle of virtual work that the reaction forces conjugate to the generalized degrees of freedom represent the nine components of the macroscopic first Piola stress, also denoted with an overbar, i.e.,

$$[\bar{\mathbf{S}}] = \begin{bmatrix} \bar{S}_{11} & \bar{S}_{12} & \bar{S}_{13} \\ \bar{S}_{21} & \bar{S}_{22} & \bar{S}_{23} \\ \bar{S}_{31} & \bar{S}_{32} & \bar{S}_{33} \end{bmatrix}. \quad (3.4)$$

Thus, the micromechanical modeling approach is able to predict the macroscopic response under any homogeneous state of deformation with the macroscopic state prescribed through a combination of displacement gradient and first Piola stress components.

In order to determine the isotropic, ground-state shear modulus of the composite material in our micromechanical simulations, we subject each RVE to simple tension along each of the three Cartesian directions. Simple tension is achieved by applying a small uniaxial strain of 1% (e.g., $\bar{H}_{11} = 0.01$ for simple tension in the 1-direction), while all stress components, except that one conjugate to the applied strain (\bar{S}_{11} for simple tension in the 1-direction), are maintained at zero. Since the matrix is

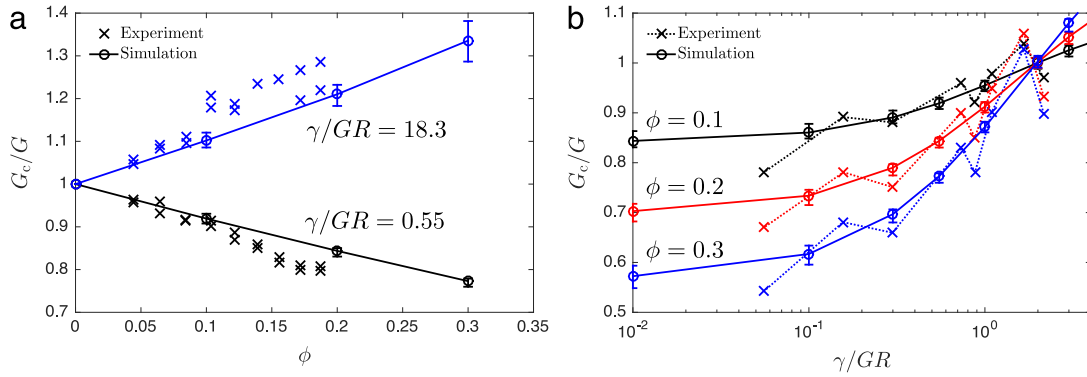


Fig. 3. (a) Normalized composite shear modulus G_c/G as a function of droplet volume fraction ϕ for two different elasto-capillary numbers, $\gamma/GR = 0.55$ and 18.3. The \circ symbols represent the simulations, and the \times symbols denote the experiments of Style et al. [20] on glycerin droplets in a silicone gel matrix. (b) Normalized composite shear modulus G_c/G as a function of elasto-capillary number γ/GR for droplet volume fractions $\phi = 0.1, 0.2$, and 0.3 . The \circ symbols represent the simulations, and the \times symbols denote the experiments of Ducloué et al. [21] on air-filled droplets in a dense emulsion matrix. The error bars on the simulation results denote the maximum and minimum values measured in our calculations, verifying that our results represent an isotropic composite. Lines are guides for the eye. (For interpretation of the references to color in this figure legend, the reader is referred to the web version of this article.)

nearly incompressible and the droplet is constrained to have fixed volume, the measured Young's modulus is simply $3G_c$ (e.g., $G_c = \bar{S}_{11}/3\bar{H}_{11}$ for simple tension in the 1-direction). Furthermore, we also subject each RVE to pure shear in each of the three Cartesian planes to obtain three additional measurements of G_c for each RVE. For example, for pure shear in the 1–2-plane, we apply $\bar{H}_{12} = \bar{H}_{21} = 0.005$ and set all other non-conjugate stress components equal to zero; the composite shear modulus is then $G_c = \bar{S}_{12}/2\bar{H}_{12}$. Therefore, with two RVEs for each volume fraction, we have 12 numerical measurements of G_c for each combination of droplet volume fraction ϕ and elasto-capillary number γ/GR under consideration. In the plotted data that follows, symbols denote the mean value of these 12 measurements, and error bars denote the full range (maximum and minimum) of the measured G_c .

Our first task is to compare our calculation results to experimental measurements from the literature. The effect of fluid-filled droplets on the infinitesimal composite modulus has been considered experimentally for glycerin droplets in a silicone gel matrix [20] and for air bubbles in a dense emulsion matrix [21]. First, considering the work of Style et al. [20], the composite shear modulus was measured for composites with average droplet size of $1\ \mu\text{m}$ and matrix shear moduli of $G = 1$ and 33 kPa as a function of droplet volume fraction, and their data is reproduced in Fig. 3(a) as blue \times symbols for the $G = 1$ kPa case and as black \times symbols for the $G = 33$ kPa case. For the case of a stiffer matrix – and hence a lower elasto-capillary number – the composite becomes more compliant with higher droplet volume fraction; however, the reverse is true for the more compliant matrix with the composite becoming stiffer for higher volume fractions of droplets. Since the droplet size R and interfacial surface tension γ remain fixed in the two cases, the ratio of the elasto-capillary numbers of the two cases must be 33. Using our simulation capability, we find that the elasto-capillary numbers that produce composite shear moduli best corresponding to the experimental data and that also maintain a ratio of 33 are $\gamma/GR = 0.55$ and 18.3.

The numerically simulated composite shear modulus for these two elasto-capillary numbers as a function of droplet volume fraction ϕ is plotted with the data of Style et al. [20] as \circ symbols. The error bars are reasonably tight, indicating that our simulations represent a good measure of the isotropic composite shear modulus.⁴ From these values of the elasto-capillary numbers along with the reported droplet size and matrix shear moduli, we may estimate the interfacial surface tension as $\gamma = 18.3\ \text{mJ/m}^2$, which is close to the value estimated by Style et al. [20] of $\gamma = 14\ \text{mJ/m}^2$. Fig. 3(b) shows a comparison of the simulated normalized composite shear modulus as a function of elasto-capillary number for droplet volume fractions of $\phi = 0.1, 0.2$, and 0.3 to the experimental data of Ducloué et al. [21] for a composite made of air bubbles in a dense emulsion matrix. The comparison remains good for a different composite material system.

Next, we compare our simulation results against two analytical theories: the Mori–Tanaka-based approach, derived by both Ducloué et al. [21] and Mancarella et al. [25], and a three-phase generalized self-consistent (GSC) theory, derived by Mancarella et al. [27]. First, for the Mori–Tanaka approach (see [25] for details of the derivation), the ground-state composite shear modulus is given through the droplet volume fraction and elasto-capillary number as

$$\frac{G_c}{G} = \frac{6 - 6\phi + (\gamma/GR)(5 + 3\phi)}{6 + 4\phi + (\gamma/GR)(5 - 2\phi)} \quad (3.5)$$

for the case of an incompressible matrix. We also consider the three-phase, generalized self-consistent approach of Mancarella et al. [27], which extended the work of Christensen and Lo [26] to include the effect of surface tension. This approach begins by considering a single droplet of radius R inside of a thick spherical shell of matrix material with shear modulus G and outer radius

⁴ In general, increased scatter is observed as the droplet volume fraction is increased.

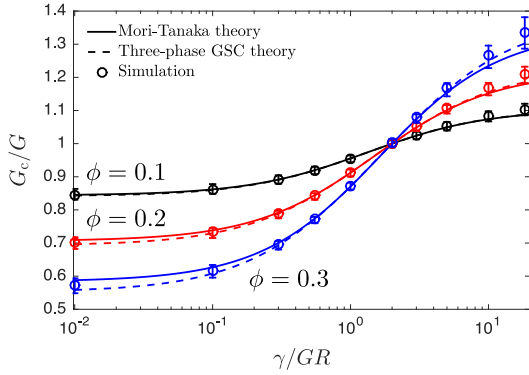


Fig. 4. Normalized composite shear modulus G_c/G as a function of elasto-capillary number γ/GR for droplet volume fractions $\phi = 0.1, 0.2$, and 0.3 . The \circ symbols represent the simulations with error bars interpreted as in Fig. 3, the solid lines denote the Mori–Tanaka-based theory (3.5) of Ducloué et al. [21] and Mancarella et al. [25], and the dashed lines denote the three-phase, generalized-self-consistent (GSC) theory of Mancarella et al. [27].

chosen to achieve the desired droplet volume fraction ϕ , which is then embedded inside of an infinite matrix of the homogenized composite material with unknown properties. Through their analysis – explicitly accounting for the interfacial surface tension γ – they determine an implicit equation for the shear modulus of the homogenized composite as a function of ϕ and γ/GR (see Equation (15) of Mancarella et al. [27]), which is quite lengthy and for the sake of brevity is not reproduced here. The two analytical models for the normalized composite shear modulus G_c/G are plotted as a function of the elasto-capillary number for droplet volume fractions of $\phi = 0.1, 0.2$, and 0.3 along with our simulation results in Fig. 4. The three approaches are consistent with one another. Namely for elasto-capillary numbers less than 2, the composite shear modulus is less than the matrix modulus with the effect being stronger for greater droplet volume fractions. The reverse is true for elasto-capillary numbers greater than 2. For an elasto-capillary number of 2, all approaches capture the “cloaking” [20] of the fluid-filled droplets for all ϕ , in which the composite material behaves identically to the homogeneous matrix material. We close by noting that while all three approaches yield quantitatively similar results, the simulations are in slightly better agreement with the three-phase GSC approach than the Mori–Tanaka theory.

3.2.2. Large deformations of composites with fluid-filled droplets

Finally, since our approach is not limited to small deformations, we turn attention to the large-deformation behavior of composites with fluid-filled droplets. First, we consider the simple tension mode of deformation – described in the previous section – for droplet volume fractions of $\phi = 0.1$ and 0.2 and elasto-capillary numbers of $\gamma/GR = 0.1, 1$, and 10 . For each combination of droplet volume fraction and elasto-capillary number, we calculate the nominal stress versus nominal strain response in simple tension, e.g., \bar{S}_{11} versus \bar{H}_{11} for simple tension in the 1-direction. As before, two RVEs are utilized, and we

consider simple tension along each of the three Cartesian directions, so that we have six sampling of the nominal stress/strain response for each of the six combinations of ϕ and γ/GR , allowing us to assess the degree of isotropy of the simulated response. The nominal stress versus nominal strain response to a maximum nominal strain of 0.45 is plotted in Fig. 5(a). The symbols and error bars have the same meanings as in the previous section, and the range of the error bars is narrow, confirming that our calculation results are representative of an isotropic response. We have normalized the nominal uniaxial stress by the infinitesimal shear modulus G_c for each combination of ϕ and γ/GR , determined in the previous section, and observe that the simulated data collapse to a single response, which is the same as the response of the homogeneous Neo-Hookean matrix material. Recall that the nominal-stress/stretch response of a homogeneous, incompressible Neo-Hookean material for simple tension in the 1-direction is given by

$$\frac{S_{11}}{G} = \lambda_1 - \frac{1}{\lambda_1^2}, \quad (3.6)$$

where the uniaxial stretch λ_1 is related to the nominal strain through $H_{11} = \lambda_1 - 1$. Eq. (3.6) is plotted as a dashed line in Fig. 5(a), and it passes through the simulated data. Hence, the large-deformation response of the composite material is nearly the same as the response of a homogeneous Neo-Hookean material with ground-state shear modulus $G_c(\phi, \gamma/GR)$.

To test this observation in another mode of deformation, we consider *simple shear* for the same six combinations of ϕ and γ/GR . For simple shear in the 1–2-plane, the macroscopic displacement gradient is specified as

$$[\bar{\mathbf{H}}] = \begin{bmatrix} 0 & \bar{H}_{12} & 0 \\ 0 & 0 & 0 \\ 0 & 0 & 0 \end{bmatrix}, \quad (3.7)$$

where \bar{H}_{12} denotes the amount of shear, which gives rise to a nominal shear stress \bar{S}_{12} . The nominal shear stress versus amount of shear response is calculated for simple shear in each of the three Cartesian planes for each of the two RVEs, so that the isotropy of the calculated response may be confirmed. This response is plotted in Fig. 5(b) for all six combinations of ϕ and γ/GR considered previously for simple tension and to a maximum amount of shear of 0.8 , and the response appears isotropic. The nominal shear stress is normalized by the ground-state shear modulus for each case, and the data again collapses to a single response. For a homogeneous Neo-Hookean material, the relation between nominal shear stress and amount of shear is simply linear, i.e., $S_{12}/G = H_{12}$ for simple shear in the 1–2-plane. This linear relationship is plotted as a dashed line in Fig. 5(b), again passing through the data and demonstrating that the composite material behaves as a homogeneous Neo-Hookean material with ground-state shear modulus $G_c(\phi, \gamma/GR)$.

The observations of the preceding paragraphs suggest that the homogenized composite material may be modeled as a hyperelastic material with free energy density function identical in form to that of the matrix material but with the

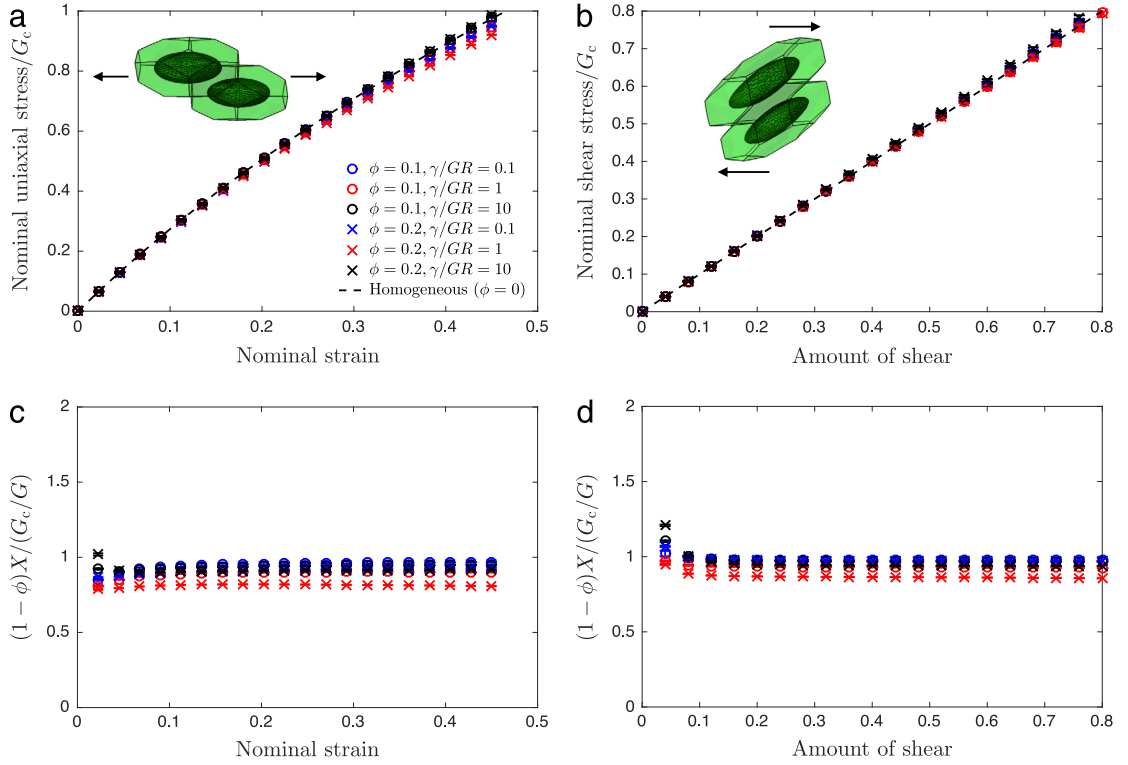


Fig. 5. Simulated large-deformation response of composites with fluid-filled droplets for droplet volume fractions of $\phi = 0.1$ and 0.2 and elasto-capillary numbers of $\gamma/GR = 0.1, 1$, and 10 . (a) Normalized nominal stress versus nominal strain in simple tension and (b) normalized nominal shear stress versus amount of shear in simple shear. Insets show the deformed mesh for the $\phi = 0.2$ and $\gamma/GR = 0.1$ case at the maximum levels of deformation for each loading mode. Normalized deformation amplification factor, $(1 - \phi)X/(G_c/G)$, as a function of deformation in (c) simple tension and (d) simple shear. Symbols and error bars are interpreted as in Fig. 3.

ground-state shear modulus of the matrix G replaced by $G_c(\phi, \gamma/GR)$. Denoting the composite free energy per unit total volume (including the droplet volume) as ψ_c , we have that

$$\psi_c = \frac{1}{2} G_c(\phi, \gamma/GR) (I_1 - 3), \quad (3.8)$$

where for simplicity, we have idealized the composite material as *incompressible* and hence do not consider a volumetric contribution to the composite free energy density. Here, I_1 denotes the *macroscopic* first stretch invariant – in the context of our previous composite simulations, I_1 is obtained through the macroscopic deformation \mathbf{H} .

In order to obtain an understanding of the observed form of the composite free energy density function (3.8), we invoke the physical picture of deformation amplification in the matrix, introduced by Bergström and Boyce [32] in the context of particle-filled elastomers. For a composite material – be it a particle-filled elastomer or a soft solid with fluid-filled inclusions – deformation in the matrix is inhomogeneous, and the average amount of deformation in the matrix is different from the applied macroscopic deformation. Further, since fluid-filled inclusions – like rigid filler particles – do not themselves contribute to the strain energy, the total strain energy of the composite material is simply due to the strain energy generated by deformation in the matrix material.

Hence, we expect the Bergström–Boyce approach to be applicable to soft solids with fluid-filled inclusions as well.

The key point of the deformation-amplification approach of Bergström and Boyce [32] is to quantify the deformation in the matrix through the volume-averaged first stretch invariant, denoted as

$$\langle I_1 \rangle = \frac{1}{V_m} \int_{V_m} I_1 dv, \quad (3.9)$$

where V_m is the volume of the matrix phase. Then, with ψ denoting the free energy density of the Neo-Hookean matrix material, ψ_c is given through

$$\psi_c = (1 - \phi) \psi(\langle I_1 \rangle) = \frac{1}{2} (1 - \phi) G(\langle I_1 \rangle - 3). \quad (3.10)$$

Bergström and Boyce [32] then postulated that $\langle I_1 \rangle$ could be related to the macroscopically applied I_1 through a simple, *deformation-independent* amplification factor, X (not to be confused with the referential coordinate), i.e., $\langle I_1 \rangle = X(I_1 - 3) + 3$. In Bergström and Boyce [32], X was taken to depend only upon the volume fraction of filler particles and was only greater than one, but here, we allow X to depend upon both the droplet volume fraction ϕ and the elasto-capillary number γ/GR and to take values both greater than and less than one. Hence, the composite free energy density function may be written in terms of X and

I_1 as

$$\psi_c = (1 - \phi)\psi(I_1) = \frac{1}{2}(1 - \phi)GX(\phi, \gamma/GR)(I_1 - 3). \quad (3.11)$$

In order for (3.8) and (3.11) to be consistent with one another, the I_1 -amplification factor should be given through the ground-state composite shear modulus by

$$X(\phi, \gamma/GR) = \frac{1}{1 - \phi} \frac{G_c(\phi, \gamma/GR)}{G}. \quad (3.12)$$

To test the validity of the microscopic picture of deformation amplification – in particular, the deformation-independence of X – in our micromechanical simulations, we have also calculated the volume average of the first stretch invariant in the matrix, $\langle I_1 \rangle$, as a function of deformation for both simple tension and simple shear and for all six combinations of ϕ and γ/GR previously simulated – leading to a direct calculation of the amplification factor through $X = (\langle I_1 \rangle - 3)/(I_1 - 3)$. Hence, both sides of (3.12) have been independently measured in our simulations. Fig. 5(c) and (d) show the normalized amplification factor $(1 - \phi)X/(G_c/G)$ as a function of deformation for simple tension and simple shear, respectively. This ratio remains close to unity and independent of deformation in all cases, showing that the deformation amplification approach – originally proposed for elastomers filled with rigid particles – indeed remains valid for the case of elastomers with fluid-filled droplets. In summary, the large-deformation response of these composite materials may be understood as follows. The presence of fluid-filled droplets at a given volume fraction and elasto-capillary number modifies the average deformation in the matrix – quantified through the volume-averaged first stretch invariant – which may be either greater than or less than the applied macroscopic deformation. However, the amount of matrix I_1 -amplification does not depend upon the amount of macroscopic deformation – a key observation in our micromechanical simulations. This observation enables us to relate the amplification factor to the ground-state composite shear modulus through (3.12) and to rationalize the collapse of the large-deformation response seen in Fig. 5(a) and (b) and the form of the composite free energy density (3.8).

4. Conclusion

In this work, we have extended our finite-element approach for elasto-capillary problems [28] to three-dimensional settings – in particular, a ten-node quadratic tetrahedral element and an eight-node linear hexahedral element have been implemented in Abaqus/Standard [33] as user-element (UEL) subroutines, which have been made available online. The three-dimensional numerical simulation capability has been applied to a class of fluid-filled droplet inclusion problems, including the response of isolated fluid-filled droplets in a soft solid matrix as well as composite materials with finite volume fractions of fluid-filled droplets under both small and large deformations. We obtain excellent agreement between our simulation results and the experiments of Style et al. [20] and

Ducloué et al. [21] for both isolated droplets and composite materials. The simulation results also agree well with theoretical predictions of the ground-state shear modulus of the composite material based on both the Mori–Tanaka theory [21,25] and the three-phase GSC theory [27]. Since our simulation capability makes no linearizing assumptions, it may be used to model the response of the composite material under large deformations. For this case, we have shown that the response of the composite material for different droplet volume fractions and elasto-capillary numbers may be collapsed by normalizing the nominal stress by the infinitesimal shear modulus of the composite material – motivating a free energy density function for the composite material consistent with the deformation amplification approach of Bergström and Boyce [32]. Looking forward, we expect our simulation capability to aid in the modeling of elasto-capillary phenomena in complex geometries. Further, our simulation platform may be straightforwardly extended to situations in which the surface energy density is deformation-dependent [4,5,2] – an issue that will be the subject of future work.

Acknowledgments

DLH acknowledges funds from the Brown University School of Engineering and an ASME AMD Haythornthwaite Research Initiation Grant. Discussions with Ethan Parsons are gratefully acknowledged.

References

- [1] B. Andreotti, O. Bäumchen, F. Boulogne, K.E. Daniels, E.R. Dufresne, H. Perrin, T. Salez, J.H. Snoeijer, R.W. Style, Soft capillarity: when and how does surface tension deform soft solids? *Soft Matter* 12 (2016) 2993–2996.
- [2] R.W. Style, A. Jagota, C.-Y. Hui, E.R. Dufresne, Elastocapillarity: Surface tension and the mechanics of soft solids, 2016. arXiv:1604.02052 [cond-mat.soft].
- [3] M.E. Gurtin, A.I. Murdoch, A continuum theory of elastic material surfaces, *Arch. Ration. Mech. Anal.* 57 (1975) 291–323.
- [4] P. Steinmann, On boundary potential energies in deformational and configuration mechanics, *J. Mech. Phys. Solids* 56 (2008) 772–800.
- [5] A. Javili, P. Steinmann, A finite element framework for continua with boundary energies. Part II: The three-dimensional case, *Comput. Methods Appl. Mech. Engrg.* 199 (2010) 755–765.
- [6] S. Mora, C. Maurini, T. Phou, J.-M. Fromental, B. Audoly, Y. Pomeau, Solid drops: Large Capillary deformations of immersed elastic rods, *Phys. Rev. Lett.* 111 (2013) 114301.
- [7] D. Paretkar, X. Xu, C.-Y. Hui, A. Jagota, Flattening of a patterned compliant solid by surface stress, *Soft Matter* 10 (2014) 4084–4090.
- [8] S. Mora, Y. Pomeau, Softening of edges of solids by surface tension, *J. Phys.: Condens. Matter* 27 (2015) 194112.
- [9] R.W. Style, C. Hyland, R. Boltyanskiy, J.S. Wettlaufer, E.R. Dufresne, Surface tension and contact with soft elastic solids, *Nature Commun.* 4 (2013) 2728.
- [10] X. Xu, A. Jagota, C.-Y. Hui, Effects of surface tension on the adhesive contact of a rigid sphere to a compliant substrate, *Soft Matter* 10 (2014) 4625–4632.
- [11] K.E. Jensen, R. Sarfati, R.W. Style, R. Boltyanskiy, A. Chakrabarti, M.K. Chaudhury, E.R. Dufresne, Wetting and phase separation in soft adhesion, *Proc. Natl. Acad. Sci.* 112 (2015) 14490–14494.
- [12] C.-Y. Hui, T. Liu, T. Salez, E. Raphael, A. Jagota, Indentation of a rigid sphere into an elastic substrate with surface tension and adhesion, *Proc. R. Soc. Lond. Ser. A Math. Phys. Eng. Sci.* 471 (2015) 20140727.
- [13] S. Mora, T. Phou, J.-M. Fromental, L.M. Pismen, Y. Pomeau, Capillarity driven instability of a soft solid, *Phys. Rev. Lett.* 105 (2010) 214301.
- [14] J.A. Zimmerman, N. Sanabria-DeLong, G.N. Tew, A.J. Crosby, Cavitation rheology for soft materials, *Soft Matter* 3 (2007) 763–767.

- [15] S. Kundu, A.J. Crosby, Cavitation and fracture behavior of polyacrylamide hydrogels, *Soft Matter* 5 (2009) 3963–3968.
- [16] S.B. Hutchens, A.J. Crosby, Soft-solid deformation mechanics at the tip of an embedded needle, *Soft Matter* 10 (2014) 3679–3684.
- [17] D. Chen, S. Cai, Z. Suo, R.C. Hayward, Surface energy as a barrier to creasing of elastomer films: An elastic analogy to classical nucleation, *Phys. Rev. Lett.* 109 (2012) 038001.
- [18] S. Mora, M. Abkarian, H. Tabuteau, Y. Pomeau, Surface instability of soft solids under strain, *Soft Matter* 7 (2011) 10612–10619.
- [19] S. Seifi, H.S. Park, Computational modeling of electro-elasto-capillary phenomena in dielectric elastomers, *Internat. J. Solids Structures* 87 (2016) 236–244.
- [20] R.W. Style, R. Boltyanskiy, B. Allen, K.E. Jensen, H.P. Foote, J.S. Wettlaufer, E.R. Dufresne, Stiffening solids with liquid inclusions, *Nat. Phys.* 11 (2015) 82–87.
- [21] L. Dulcoué, O. Pitois, J. Goyon, X. Chateau, G. Ovarlez, Coupling of elasticity to capillarity in soft aerated materials, *Soft Matter* 10 (2014) 5093–5098.
- [22] J.D. Eshelby, The determination of the elastic field of an ellipsoidal inclusion, and related problems, *Proc. R. Soc. Lond. Ser. A Math. Phys. Eng. Sci.* 241 (1957) 376–396.
- [23] R.W. Style, J.S. Wettlaufer, E.R. Dufresne, Surface tension and the mechanics of liquid inclusions in compliant solids, *Soft Matter* 11 (2015) 672–679.
- [24] T. Mori, K. Tanaka, Average stress in matrix and average elastic energy of material with misfitting inclusions, *Acta Metall.* 21 (1973) 571–574.
- [25] F. Mancarella, R.W. Style, J.S. Wettlaufer, Surface tension and the Mori-Tanaka theory of non-dilute soft composite solids, *Proc. R. Soc. Lond. Ser. A Math. Phys. Eng. Sci.* 472 (2016) 20150853.
- [26] R.M. Christensen, K.H. Lo, Solutions for effective shear properties in three phase sphere and cylinder models, *J. Mech. Phys. Solids* 27 (1979) 315–330.
- [27] F. Mancarella, R.W. Style, J.S. Wettlaufer, Interfacial tension and a three-phase generalized self-consistent theory of non-dilute soft composite solids, *Soft Matter* 12 (2016) 2744–2750.
- [28] D.L. Henann, K. Bertoldi, Modeling of elasto-capillary phenomena, *Soft Matter* 10 (2014) 709–717.
- [29] M. Danielsson, D.M. Parks, M.C. Boyce, Three-dimensional micromechanical modeling of voided polymeric materials, *J. Mech. Phys. Solids* 50 (2002) 351–379.
- [30] M. Danielsson, D.M. Parks, M.C. Boyce, Micromechanics, macromechanics and constitutive modeling of the elasto-viscoplastic deformation of rubber-toughened glassy polymers, *J. Mech. Phys. Solids* 55 (2007) 533–561.
- [31] E.M. Parsons, Mechanics of large-strain deformation of particle-modified polymers (Ph.D. dissertation), MIT, 2006.
- [32] J.S. Bergström, M.C. Boyce, Mechanical behavior of particle filled elastomers, *Rubber Chem. Technol.* 72 (1999) 633–656.
- [33] Abaqus, 2015. Reference Manuals.